nature materials

Article

https://doi.org/10.1038/s41563-026-02703-6

Molecular coordination achieves uniform kesterite absorber film for efficient solar modules

Received: 16 December 2025

Accepted: 8 July 2026

Published online: 03 August 2026

Check for updates

Bowen Zhang[1,2,6], Menghan Jiao[1,2,6], Xiao Xu[1,6], Jiazheng Zhou[1,6], Jinlin Wang[1], Tan Guo[1,3], Yuan Li[1], Jingchen Wang[1,2], Shudan Chen[1,2], Yiming Li[1], Jiangjian Shi[1] ✉, Huijue Wu[1], Yanhong Luo[1,2,4], Dongmei Li[1,2,4] & Qingbo Meng[1,2,4,5] ✉

Environmentally benign and earth-abundant kesterite $Cu_2ZnSn(S,Se)_4$ (CZTSSe) solar cells have advanced rapidly through solution-based processing. However, scaling from laboratory-scale devices to modules remains a major challenge, largely because complex coordination networks in the precursors hinder the formation of uniform large-area films. Here we show that molecular-level regulation of metal–organic coordination can suppress the formation of cross-linked networks in precursor solutions, promoting efficient solvent removal and uniform selenization and crystallization. This coordination-controlled strategy enables the blade coating of highly homogeneous films over 10 cm^2, realizing certified efficiencies of 14.2% for 1 cm^2 cells and 13.0% for 10.5 cm^2 modules, representing a leap-forward improvement in scalable kesterite photovoltaics. Beyond performance, the provided molecular insights into kesterite solution chemistry facilitate establishing a scalable and low-cost route towards industrial deployment of this thin-film solar technology.

Kesterite $Cu_2ZnSn(S,Se)_4$ (CZTSSe) is one of the most attractive candidates for thin-film photovoltaics due to its earth-abundant and non-toxic composition, chemical stability, radiation hardness and strong industrial compatibility[1–7]. In particular, the narrow bandgap and elemental abundance of CZTSSe make it well suited as bottom cells for all-thin-film tandem photovoltaics, offering a promising route for high-efficiency, lightweight and flexible applications such as space photovoltaics[8]. Currently, laboratory CZTSSe devices have achieved certified power conversion efficiencies (PCEs) exceeding 15%, demonstrating compelling commercialization potential[9–11]. Moving from laboratory-scale cells to large-area devices and modules is thus now essential to validate their manufacturability[12,13].

Early module development by Solar Frontier using vacuum sputtering delivered continuous performance gains, reaching 11.8% for 10 cm^2 modules[14–16], and larger >20 cm^2 modules have also been reported[17]. However, progress has since plateaued, limited by efficiency bottlenecks in vacuum-processed kesterite. Meanwhile, advancing solution-processed CZTSSe devices has opened new opportunities: IBM (International Business Machines Corporation) demonstrated a nine-cell module via spin coating (~7.5% efficiency)[18], and most recently, certified efficiencies above 10% have been reported[19]. Yet substantial efficiency losses persist upon scaling, revealing the difficulty of transferring the intrinsic advantages of solution processing from small cells to large-area modules[20].

[1]Beijing National Laboratory for Condensed Matter Physics, Renewable Energy Laboratory, Institute of Physics, Chinese Academy of Sciences (CAS), Beijing, P. R. China. [2]School of Physical Sciences, University of Chinese Academy of Sciences, Beijing, P. R. China. [3]College of Materials Science and Optoelectronic Technology, University of Chinese Academy of Sciences, Beijing, P. R. China. [4]Songshan Lake Materials Laboratory, Dongguan, P. R. China. [5]Center of Materials Science and Optoelectronics Engineering, University of Chinese Academy of Sciences, Beijing, P. R. China. [6]These authors contributed equally: Bowen Zhang, Menghan Jiao, Xiao Xu, Jiazheng Zhou. ✉e-mail: shijj@iphy.ac.cn; qbmeng@iphy.ac.cn

https://doi.org/10.1038/s41563-026-02703-6

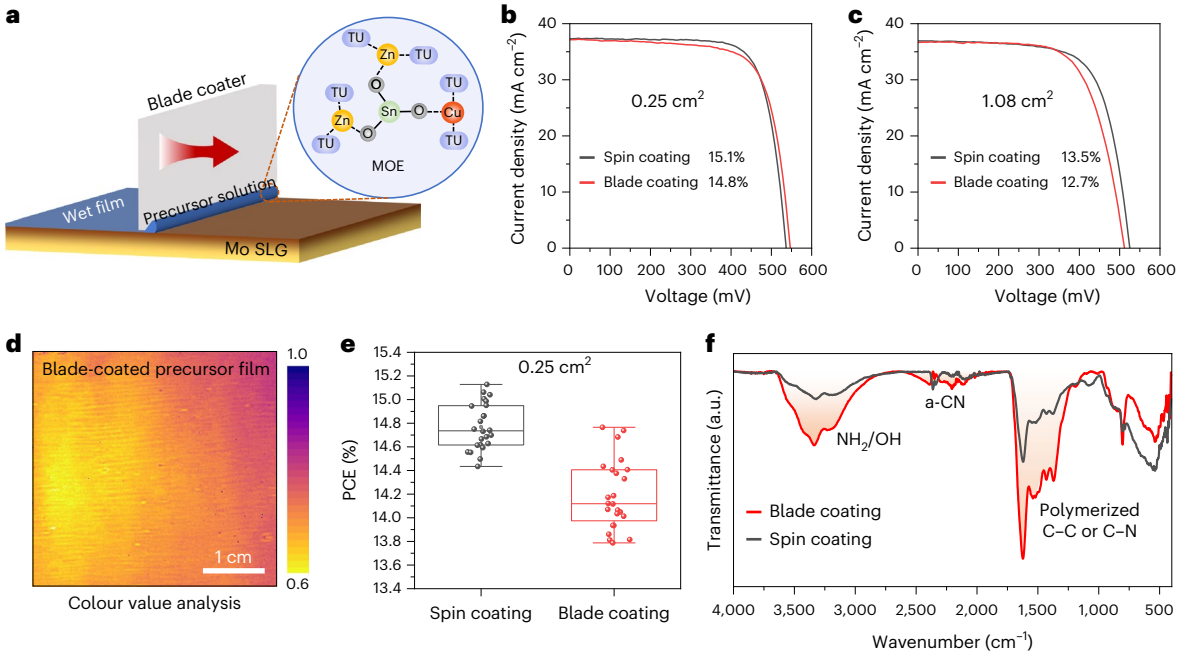

Fig. 1 | Blade coating of CZTSSe films. a, Schematic diagram of the blade coating of Cu–Zn–Sn–S wet precursor films on Mo soda lime glass (SLG) substrates. The metal ion–organic molecule coordination networks are schematically depicted. TU, Thiourea. **b**,**c**, Current–voltage characteristics of 0.25 cm^2 (**b**) and 1.08 cm^2 (**c**) cells fabricated based on blade- or spin-coating methods, respectively. **d**, Colour value analysis (HSV (hue, saturation, value) colour model) of the 4 × 4 cm blade-coated precursor film, exhibiting macroscopically visible inhomogeneity. **e**, Statistical analysis of PCEs of small-area devices prepared from the coated 4 × 4 cm films. The centre line indicates the median; box limits represent the 25th and 75th percentiles; whiskers extend to 1.5× the interquartile range; raw data points are shown. Each box contains 24 individual solar cells. **f**, Fourier transform infrared spectra of precursor films fabricated via blade- or spin-coating methods. The shaded regions at 1,200–1,700 cm^{-1}, 2,000–2,500 cm^{-1} and 2,900–3,600 cm^{-1} highlight absorption bands arising from polymerized C–C/C–N networks and OH groups.

A central barrier arises from the complex coordination chemistry of CZTSSe precursors, particularly in the low-toxic organic solutions, which exhibit multiple metal–organic structures and uncontrolled transformations during drying and crystallization[19,21–28]. These cause severe non-uniformities in solvent evaporation, coordination restructuring and nucleation, fundamentally limiting the use of standard spin-coating precursor formulations in scalable coating technologies such as doctor-blading and slot-die coating for CZTSSe preparation, where requirements on wettability, nucleation uniformity and evaporation behaviour are far more stringent[29,30]. Therefore, understanding and regulating the solution chemistry of precursors are crucial for CZTSSe coatings, and are thus driving the development of various solvent systems[31]. Among them, 2-methoxyethanol (MOE) is widely regarded as one of the most successful solvents for achieving high-efficiency CZTSSe devices and has also been demonstrated to be compatible with large-area coating processes[32,33]. However, its two coordination donors can lead to chelation, bridging and even more complex coordination networks[34–36], which may still hinder the uniform fabrication of large-area films.

Here we introduce molecular-level strategies to precisely regulate metal–organic coordination in MOE-based CZTSSe precursor solutions, enhancing their compatibility with scalable film deposition. Specifically, formamide (FA) has been introduced as a coordination additive into the solution system. Compared with MOE, FA has a shorter chain length and a single C=O coordination donor, enabling simple molecular coordination with metal ions, avoiding the formation of the aforementioned complex structures. The resulting molecularly uniform and dynamically exchangeable coordination structure enables high-quality blade coating of CZTSSe films over 10 cm^2, further allowing us to achieve certified PCEs of 14.2% and 13.0% in 1 cm^2 cells and 10.5 cm^2 modules, respectively. This represents a leap-forward improvement in scalable kesterite photovoltaics and establishing a viable pathway towards the industrialization of solution-processed CZTSSe technologies.

Large-area CZTSSe film coating

We began by blade-coating CZTSSe films at a 10 cm^2 scale. This method is suitable for nanometre- to micrometre-thick film depositions and provides a seamless transition to industrial-scale slot-die coating[29,37,38]. An MOE solution system was used due to its ambient compatibility and proven ability to produce high-performance devices[21,23,39,40]. The precursor solution was blade-coated onto cleaned Mo glasses (Fig. 1a), annealed in air and then selenized to form CZTSSe absorbers.

Cells of 0.25 cm^2 and 1.08 cm^2 were then fabricated (Fig. 1b,c and Supplementary Figs. 1 and 2). The 0.25 cm^2 blade-coated device reached 14.8% PCE, close to the best reported values, but lower than spin-coated devices, particularly in fill factor (FF; 0.73 versus 0.75). Scaling to 1.08 cm^2 further amplified the efficiency gap, with a noticeable drop in open-circuit voltage (V_{OC}), reflecting limitations in film uniformity. Visual analysis of a 4 × 4 cm blade-coated precursor film revealed this inhomogeneity along the coating direction (Fig. 1d, Supplementary Note 1 and Supplementary Fig. 3), and small-area (0.25 cm^2) devices cut from this film showed large efficiency variations (>1%; Fig. 1e), substantially higher than their spin-coated counterparts.

To understand the origin of these performance differences, we analysed blade- and spin-coated precursor films using Fourier transform infrared (FTIR) spectroscopy. Blade-coated films exhibited stronger absorption bands at 1,200–1,700 cm^{-1}, 2,000–2,500 cm^{-1} and 2,900–3,600 cm^{-1} (Fig. 1f), corresponding to polymerized C–C/C–N networks and OH groups[41]. This indicates higher levels of residual organics, probably owing to limited solvent evaporation in the relatively static wet-film coating process[34]. These polymerized networks are thermally stable, thus hindering elemental diffusion and crystal growth during selenization. At larger scales, such

limitations are amplified, producing macroscopic non-uniformities and constraining scalable device performance. Ab initio molecular dynamics (AIMD) simulations indicate that alcoholysis between MOE and $SnCl_4$, combined with MOE's dual O-coordination sites, tightly link Sn centres via bridging MOE molecules (Supplementary Note 2, Supplementary Fig. 4 and Supplementary Figs. 7 and 8). The cross-link of these metal–organic coordination could form large networks in solution, suppressing the removal of the solvent and other ligands and resulting in organic polymerization in precursor films. For Cu and Zn cations, they mainly coordinate with monodentate donors such as thiourea or chloride ions (Supplementary Figs. 9 and 10) and contribute little to the formation of crosslinked coordination networks[28,42–45]. Therefore, here we focus primarily on Sn–organics coordination.

Molecular coordination regulation of precursor solution

To address the above issue, FA was introduced to replace the ligand role of MOE. Experimentally, $SnCl_4$ was first dissolved in FA, followed by the addition of MOE solely as a solvent. The effectiveness of this strategy was first assessed using AIMD simulations (Supplementary Note 2 and Supplementary Figs. 4–8). The results indicate that FA forms simple, non-crosslinked complexes with Sn. Specifically, in the pure FA–Sn solution, Sn is coordinated by the carbonyl O atoms in FA, forming isolated metal–organic complexes. The N atoms rarely participate in coordination because of steric hindrance from surrounding H atoms. After introducing MOE, the coordination environment remains dominated by FA, while most FA and MOE molecules remain uncoordinated and mainly function as solvents, as illustrated in Fig. 2a.

This conclusion is further supported by statistical analysis of the AIMD trajectories within the 100–300 ps time window, including radial distribution functions and coordination numbers (Supplementary Fig. 7). In the mixed solution, Sn primarily coordinates with O atoms in FA with a coordination number of ~6, and weakly with Cl atoms (~1), whereas the O atoms from MOE contribute nearly zero coordination (Fig. 2b). Under this coordination environment, the Sn–FA complexes in the mixed solvent maintain dynamic ligand-exchange behaviour. This is evidenced by the continuous breaking and re-forming of Sn–O bonds during 100–300 ps, reflected by the decreasing survival probability of Sn–O coordination, similar to the pure FA system. In contrast, the survival probability of Sn–O coordination remains unity in the pure MOE solution, indicating almost no ligand-exchange dynamics due to the formation of a rigid, crosslinked Sn–MOE coordination cluster (Fig. 2c). Sn K-edge X-ray absorption fine structure (EXAFS) spectroscopy was further performed on the Sn–MOE, Sn–FA and Sn–FA/MOE solutions, yielding results consistent with the AIMD calculations. The Sn–FA and Sn–FA/MOE systems show nearly identical EXAFS features (Supplementary Fig. 11), clearly distinct from those of Sn–MOE, indicating similar structures dominated by Sn–FA coordination. Fourier transform analysis further shows comparable coordination shells for Sn–FA and Sn–FA/MOE, whereas Sn–MOE exhibits a markedly stronger and narrower first-shell peak, suggesting a more rigid coordination configuration likely associated with reduced ligand dynamic exchange[46–48], consistent with AIMD predictions.

We further probed the coordination environment in solution using NMR spectroscopy[49] (Fig. 2d). In the ^{13}C NMR of pure MOE solutions, Sn coordination causes clear chemical shifts, including ~0.22 ppm downfield and ~0.7 ppm upfield shifts in hydroxyl-adjacent and ether carbon signals, respectively. These shifts are consistent with strong alcoholysis-driven coordination and possible Cl^- participation in anionic complexes[27,50]. Peak broadening and the complete shift of these signals suggest that nearly all MOE molecules participate in extended coordination networks, even at MOE/Sn ratios >12. Conversely, FA–Sn coordination generates a new ~3.1 ppm downfield peak while retaining the free FA signal, reflecting the coexistence of coordinated and uncoordinated FA. In the FA–MOE mixed system, FA exhibits similar shifts whereas MOE shows no coordination-related changes. The ^{119}Sn NMR spectra further support these observations: FA–MOE mixed solutions retain the distinct resonance signature of FA–Sn coordination, whereas the broad resonance associated with MOE-derived networks disappears[51]. These results confirm that FA acts as the coordinating ligand while MOE functions mainly as a solvent, consistent with the simulation results.

Raman spectroscopy further confirms the ligand-exchange dynamics in these systems. MOE-based solutions with multiple metal cations exhibit prominent Sn-related peaks, reflecting a solidified Sn–MOE coordination structure. In contrast, FA-based solutions show broad baseline-like spectra indicative of dynamic ligand exchange and continuous coordination rearrangement[52,53] (Supplementary Fig. 12). These simulation and spectroscopic results validate our coordination-regulation strategy, demonstrating that FA effectively regulates Sn from rigid crosslinked networks into a dynamic, non-crosslinked coordination environment. This environment favours improved molecular-level homogeneity of the kesterite precursor solution.

The macroscopic effect of this regulation is immediately evident from the Tyndall effect. MOE-only solutions (control) show gel-like heterogeneous scattering and unstable laser beams, whereas FA-containing solutions (target) exhibit uniform and weaker scattering (Fig. 2e and Supplementary Fig. 13), indicating substantially smaller colloidal structures. Dynamic light scattering further confirms that colloid sizes in FA-containing solutions are one to two orders of magnitude smaller (Fig. 2f). This reflects a simpler coordination environment and better molecular dispersion, which is also supported by the lower solution viscosity (Supplementary Note 3 and Supplementary Fig. 14).

We further used FTIR spectroscopy to investigate how the altered coordination structure and solution chemistry influence the properties of organic species in precursor films prepared from these solutions. During sample preparation, a low-temperature (~120 °C) vacuum-drying process was used to remove free solvent. The results (Fig. 2g) reveal pronounced C–H vibrations in MOE–Sn films, indicating significant MOE residues. Meanwhile, their ether and hydroxyl C–O vibrations are suppressed and shifted, consistent with incorporation into a solidified MOE–Sn coordination network that restricts molecular structural freedom and volatilization. In contrast, FA-dominated systems, including both pure FA and FA–MOE mixtures, show only FA–Sn coordination signals, with no detectable MOE- or free FA-related vibrations. This demonstrates efficient removal of organic solvents during drying[54]. Overall, FA-mediated coordination control enhances organic removal during film formation, minimizing residual species that could otherwise compromise CZTSSe crystallization and film uniformity.

CZTSSe film preparation and characterization

Building on this coordination-regulated solution, we next prepared CZTSSe films via blade-coating processes. As in Fig. 3a, the precursor films showed markedly improved visual uniformity, with colour distributions fitting a single Gaussian curve rather than multiple distributions observed in control samples (Fig. 3b and Supplementary Fig. 3). Thermogravimetric analysis was used to probe the metal–organic thermal decomposition occurring during precursor film formation. The control sample exhibited two distinct steps in the 180–280 °C range due to more complex decomposition pathways and products (Supplementary Figs. 15 and 16), whereas the FA-based precursor demonstrated a single and constant mass-loss process (Fig. 3c), corresponding to more uniform organic removal and structural transformation.

We next examined selenization dynamics of these coated films. FTIR spectra also confirmed the efficient removal of the organic solvent (MOE) and ligand (FA) in the target precursor films, evidenced by the disappearance of OH (3,000–3,600 cm^{-1}) and C=O (~1,700 cm^{-1}) vibrations, while residual signals remained in the control[41] (Fig. 3d).

https://doi.org/10.1038/s41563-026-02703-6

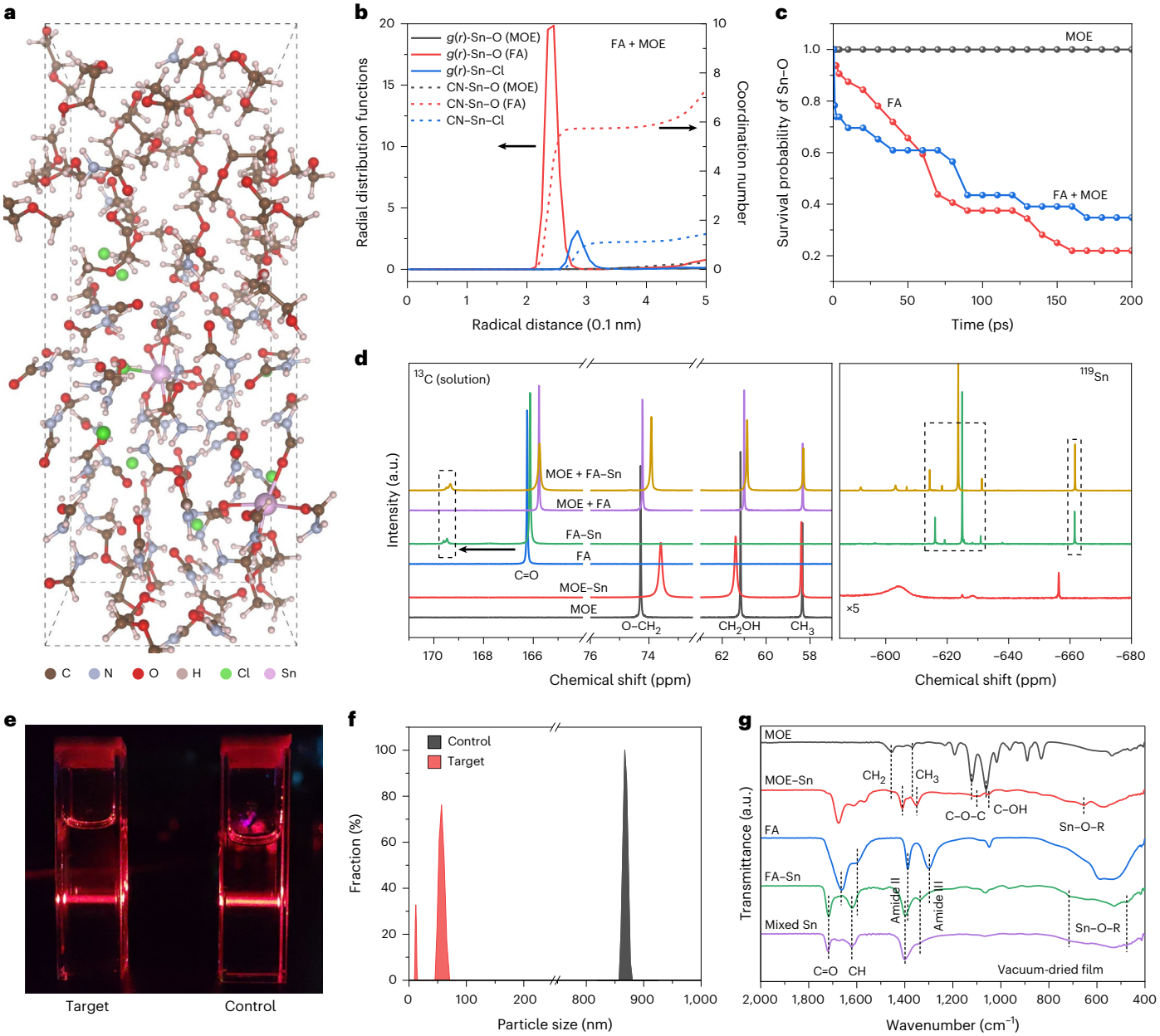

Fig. 2 | Molecular coordination regulation of precursor solutions using FA. **a**, AIMD-simulated molecular structures of the $SnCl_4$ solution in mixed FA + MOE. In this simulation, $SnCl_4$ was first dissolved in FA, forming coordination after structural evolutions for 300 ps. MOE was then added into the solution and further dynamic structural evolutions were performed for additional 300 ps. **b**, Radial distribution functions ($g(r)$) and coordination numbers (CN) of Sn–O and Sn–Cl coordination in the FA + MOE-Sn solution analysed within a time window of 100–300 ps based on the AIMD simulations. **c**, Survival probability of Sn–O coordination in MOE, FA and their mixed solutions within a time window of 100–300 ps. The continuous probability reduction in FA and FA–MOE mixed solutions indicates dynamic ligand exchange whereas the constant probability (1) means solidified Sn–O coordination in the MOE solution due to the formation of cross-linked Sn–MOE clusters. **d**, ^{13}C and ^{119}Sn NMR spectra of MOE, FA and their Sn solutions. The dashed rectangle in ^{13}C NMR spectra indicates the peaks arisen from FA–Sn coordination. The dashed rectangles in ^{119}Sn NMR spectra indicate similar peak signatures between FA–Sn and FA + MOE-Sn samples. **e**, Tyndall effect of the control (MOE) and target precursor solutions. The observed higher laser intensity in the control sample indicates stronger scattering effect. **f**, Colloidal cluster size measurement of both solutions using dynamic light scattering. **g**, FTIR spectra of vacuum-dried MOE–Sn and FA–Sn films. The spectra of liquid MOE and FA are used as references. The vertical dashed lines represent the peaks corresponding to the vibration of different organic groups.

After brief selenization (100 s), both films showed formation of amorphous CN (a-CN) networks from thiourea polymerization. However, after 600 s, the a-CN band in the target film broadened and redshifted by ~400 cm^{-1} and the C=S vibration at 800 cm^{-1} disappeared, indicating substantial softening of organic networks and more complete removal of carbonaceous residues[55].

These changes enabled faster and less constrained grain growth. Scanning electron microscopy (SEM) revealed rapid nucleation and growth of several-hundred-nanometre grains at the film bottom in the target sample, while polymer confinement preserved a fragmented structure in the control (Fig. 3e and Supplementary Fig. 17). Continued selenization produced vertically connected, dense grains in the target film, whereas the control retained abundant fine grains (Fig. 3e and Supplementary Figs. 19–21). On the final 4 × 4 cm films, the target showed uniform optical appearance, in contrast to pronounced macroscopic inhomogeneity in the control (Supplementary Fig. 18). Atomic force microscopy and SEM confirmed the formation of a compact, void-free surface in the target film, while the control

https://doi.org/10.1038/s41563-026-02703-6

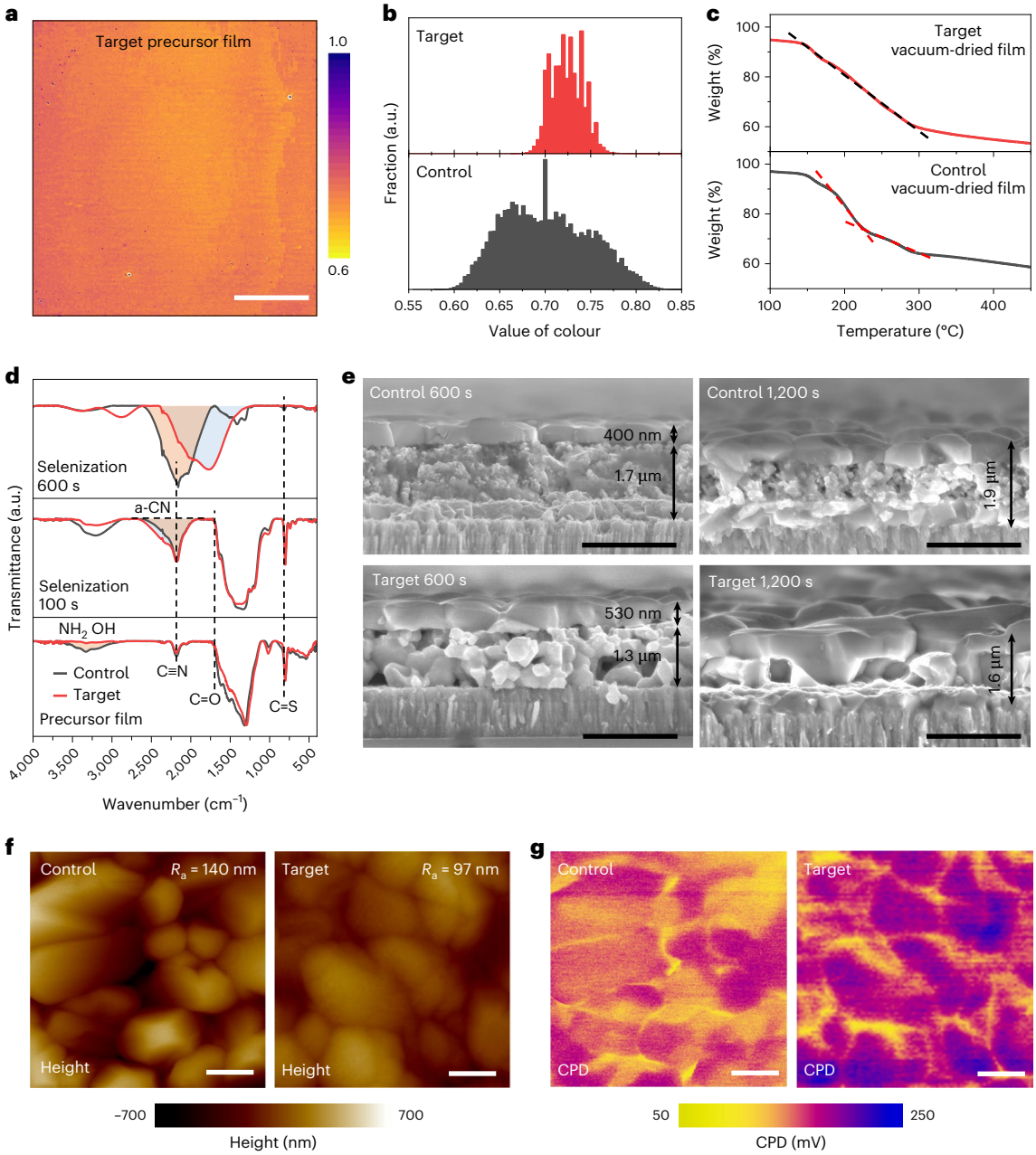

Fig. 3 | CZTSSe crystallization and film characterization. a,**b**, Colour value imaging of the blade-coated target precursor film (**a**) and the statistical distribution in the target (**b**, top) and the control (**b**, bottom). **c**, Thermogravimetric analysis of the coated films after the vacuum-drying process. The dashed lines depict the distinct stages of mass loss. **d**,**e**, FTIR spectra (**d**) and cross-sectional SEM images (**e**) of CZTSSe films at different selenization stages. **f**,**g**, Morphology (**f**) and contacting potential difference (CPD) images (**g**) of the final CZTSSe films using Kelvin probe force microscopy. R_a, average roughness. Scale bars, 1 cm (**a**), 2 µm (**e**), 1 µm (**f**,**g**).

exhibited voids originating from incomplete grain ripening (Fig. 3f and Supplementary Figs. 22 and 23). Corresponding Kelvin probe force microscopy mapping revealed pronounced potential contrast and upwards band bending at grain boundaries in the target film, which is favourable for local carrier separation near grain boundaries[56–58], while the control showed negligible contrast (Supplementary Figs. 24 and 25). Raman mapping results also support better film uniformity and quality of the target sample after selenization (Supplementary Fig. 26). These collectively demonstrate that the tailored metal–organic coordination and enhanced removal of organic-network residues promote both bulk grain growth and surface ripening of the CZTSSe film, optimizing its microstructure and optoelectronic properties.

Large-area cells and modules

Leveraging the substantial improvements in film quality and uniformity, we next fabricated devices at different scales. Small-area cells based on the FA-mediated precursor exhibited not only higher efficiencies but also significantly narrower statistical distributions compared with control devices (Fig. 4a and Supplementary Figs. 27 and 28). This performance advantage was well retained upon scaling: the 1.08 cm^2 device achieved a certified 14.2% PCE with a high FF of 0.70 (Fig. 4b and Supplementary Fig. 29). The device showed strong external quantum efficiency (EQE) across the full spectrum (Fig. 4c), corresponding to a bandgap of ~1.08 eV and an integrated short-circuit current density (J_{SC}) of 38.6 mA cm^{-2}, consistent with the total-area current–voltage (I–V) characteristics of the cell. We also characterized

https://doi.org/10.1038/s41563-026-02703-6

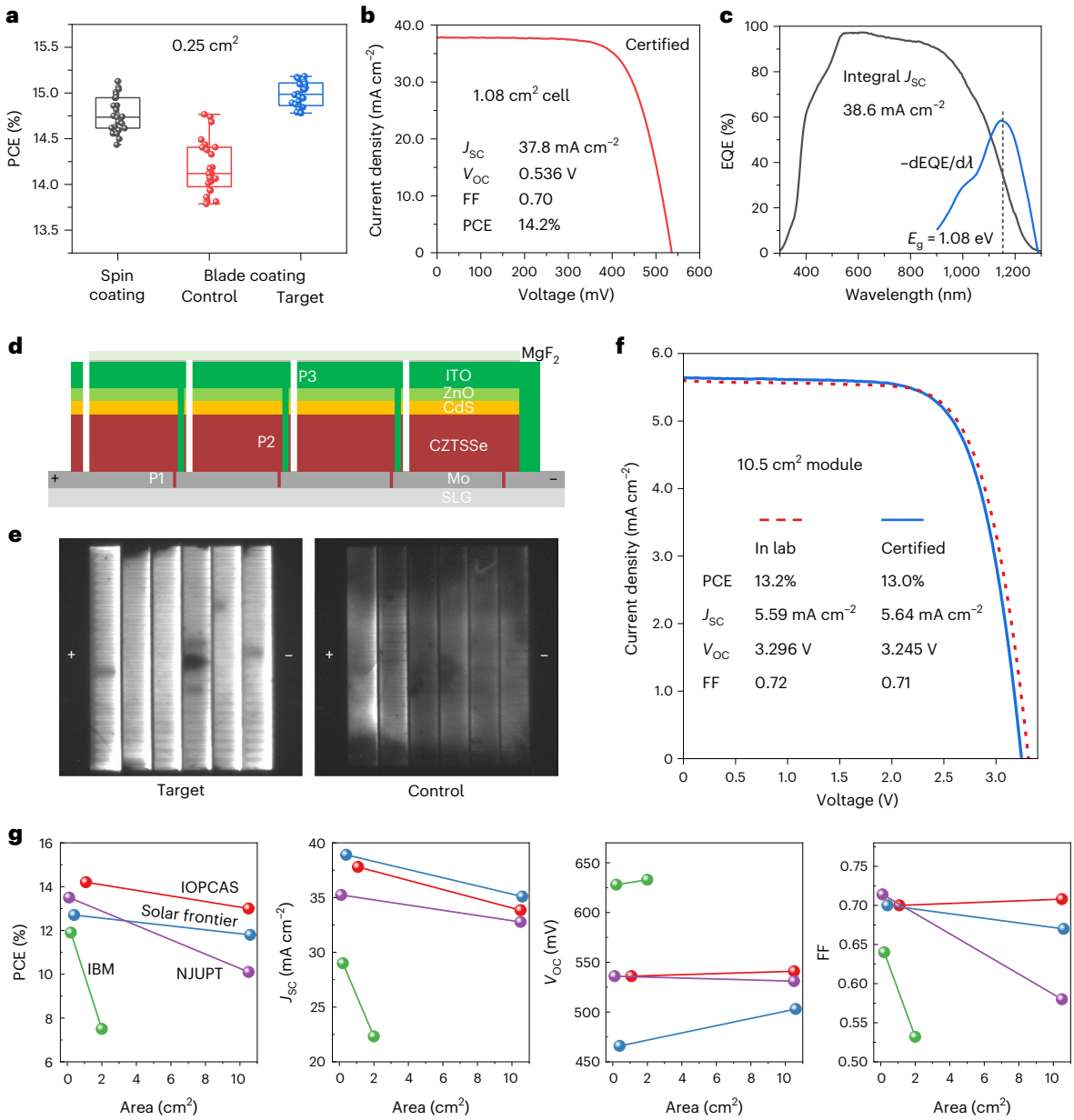

Fig. 4 | Characterization of large-area cells and series-connected modules. **a**, Statistical PCE of the small-area cells fabricated by different approaches (spin coating is based on control precursors). The centre line indicates the median; box limits represent the 25th and 75th percentiles; whiskers extend to 1.5× the interquartile range; raw data points are shown. Each box contains 24 individual solar cells. **b**, Certified *J*–*V* curve of a 1.08 cm² cell, giving a record PCE of 14.2%. **c**, EQE spectrum of the cell. The bandgap of the CZTSSe absorber was estimated at the maxima position of the differential EQE spectrum (−dEQE/dλ), which is marked up with the vertical dashed line. **d**, Schematic diagram of the laser-patterned series-connected module. **e**, Electroluminescence images of the modules (at 3.8 V) captured by a broad-spectrum camera. **f**, *J*–*V* curves of a 10.5 cm² module with six subcells measured in our lab and at the National PV Industry Measurement and Testing Center (NPVM), China, giving in-lab and certified PCEs of 13.2% and 13.0%, respectively. **g**, Evolutions of device efficiencies with areas reported by several teams. IOPCAS, Institute of Physics, Chinese Academy of Sciences.

transient photocurrent and photovoltage characteristics of these solar cells[59–62] (Supplementary Note 4 and Supplementary Figs. 30 and 31). Target devices maintained sharp and bias-independent photocurrent peaks under different biases while control devices exhibited broadened and delayed peaks under forward bias. This suggests that, across the entire operating voltage range, photogenerated carriers in the target CZTSSe show a more stable transfer into the window layer, consistent with its superior crystalline quality. For transient photovoltage, the decay characteristics of the target cells were nearly unaffected by area scaling, whereas the transient photovoltage decay in the control devices accelerated markedly with increasing area, which is also consistent with the higher uniformity of the target sample.

We further realized monolithic series-connected modules via multi-step laser scribing on 4 × 4 cm film substrates (Fig. 4d). Electroluminescence imaging directly visualized excellent uniformity of the target module over 10.5 cm² (Fig. 4e): apart from minor intensity loss near damaged grids, strong and homogeneous electroluminescence was observed throughout, with negligible variations among subcells, indicative of uniform film quality and high-quality scribing. In contrast, control modules exhibited weak and spatially heterogeneous emissions, consistent with their limited charge transport capability and film inhomogeneity.

Benefitting from these improvements, the target module realized a PCE of 13.2% in our lab. This module also achieved a certified

13.0% PCE with a J_{SC} of 5.64 mA cm^{-2} (equivalent to 33.84 mA cm^{-2} per cell), V_{OC} of 3.245 V (541 mV per cell), and an FF of 0.71 (Fig. 4f and Supplementary Fig. 32), surpassing the previous benchmark set by Solar Frontier. In particular, efficiency retention of our devices remained exceptionally high across scaling: 94% from 0.25 cm^2 to 1 cm^2 and 91% from 1 cm^2 to 10.5 cm^2, approaching the level of state-of-the-art perovskite photovoltaics[63]. They also maintained the highest reported FF values and FF retention (~96%) among all kesterite modules[16,18,19], and exhibited a small V_{OC} deficit ($E_g/e - V_{OC}$, where E_g is the bandgap and e is the elementary charge) of only 0.54 V, already close to small-area cells and significantly lower than previously reported results.

Overall, the achieved performance progress arises from several factors. Compared with the solution spin-coating approaches reported by IBM and Nanjing University of Posts and Telecommunications (NJUPT), the blade-coating process used here, together with the simplified coordination environment, enables significantly improved film uniformity. In addition, the optimized selenization and crystallization processes developed for CZTSSe films provide an important foundation for achieving high-quality absorbers[6,11,20,21,23]. Compared with the vacuum-deposition-based results reported by Solar Frontier, these results further highlight the advantages of solution processing. In particular, the more uniform distribution of metal elements in the precursor films promotes faster selenization and crystallization and reduces the likelihood of defect formation[19,31,64].

Looking ahead, further efficiency gains will require minimizing optical and resistive losses introduced during laser scribing, which remains challenging due to insufficient understanding of laser–CZTSSe–$MoSe_x$ interactions[65,66]. In addition, development of highly uniform, large-area selenization systems compatible with solution processing is essential for industrial scaling. Continued improvements in small-area CZTSSe device efficiency, achieved through deeper control of charge losses, defect physics and interfacial quality, will be critical for enabling the next stage of high-performance kesterite modules.

Outlook

In summary, we have developed a tailored metal–organic molecule coordination strategy to enable the scalable solution coating route for producing large-area CZTSSe solar cells and modules. This strategy effectively eliminates the complex coordination networks in precursors and thus facilitates organic removal along with high-quality and homogeneous selenization and crystallization over large areas. Consequently, we achieved certified efficiencies of 14.2% for 1 cm^2 cells and 13.0% for 10.5 cm^2 modules, demonstrating a significant advance in the scaling of CZTSSe thin-film photovoltaics. The molecular insight into kesterite solution chemistry also provides an important foundation towards the industrialization of solution-processed thin-film solar technologies, paving the way for earth-abundant photovoltaics to move beyond laboratory demonstrations towards reliable, manufacturable and globally scalable energy solutions.

Online content

Any methods, additional references, Nature Portfolio reporting summaries, source data, extended data, supplementary information, acknowledgements, peer review information; details of author contributions and competing interests; and statements of data and code availability are available at https://doi.org/10.1038/s41563-026-02703-6.

References

1. Polman, A., Knight, M., Garnett, E. C., Ehrler, B. & Sinke, W. C. Photovoltaic materials: present efficiencies and future challenges. *Science* **352**, aad4424 (2016).
2. Wallace, S. K., Mitzi, D. B. & Walsh, A. The steady rise of kesterite solar cells. *ACS Energy Lett.* **2**, 776–779 (2017).
3. Li, J. et al. Emergence of flexible kesterite solar cells: progress and perspectives. *NPJ Flex. Electron.* **7**, 16 (2023).
4. Yan, C. et al. Cu_2ZnSnS_4 solar cells with over 10% power conversion efficiency enabled by heterojunction heat treatment. *Nat. Energy* **3**, 764–772 (2018).
5. Gong, Y. et al. Elemental de-mixing-induced epitaxial kesterite/CdS interface enabling 13%-efficiency kesterite solar cells. *Nat. Energy* **7**, 966–977 (2022).
6. Wang, J. et al. Vacancy-enhanced cation ordering via magnesium doping to enable kesterite solar cells with 14.9% certified efficiency. *Nat. Energy* **11**, 66–75 (2026).
7. Suvanam, S. S. et al. Extreme radiation hard thin film CZTSSe solar cell. *Sol. Energy Mater. Sol. Cells* **185**, 16–20 (2018).
8. Hu, S. et al. Flexible perovskite-based multiple-junction photovoltaics. *Joule* **9**, 101870 (2025).
9. Green, M. A. et al. Solar cell efficiency tables (version 66). *Prog. Photovolt.* **33**, 795–810 (2025).
10. *Best Research-Cell Efficiency Chart* (NLR, 2026); https://www.nlr.gov/pv/cell-efficiency
11. Jiao, M. et al. Suppressing defects in Kesterite solar cells via balanced phase evolution to enable 15.1% certified record efficiency. *Joule* **10**, 102345 (2026).
12. Yang, C. et al. Achievements, challenges, and future prospects for industrialization of perovskite solar cells. *Light Sci. Appl.* **13**, 227 (2024).
13. Parvazian, E. & Watson, T. The roll-to-roll revolution to tackle the industrial leap for perovskite solar cells. *Nat. Commun.* **15**, 3983 (2024).
14. Hiroi, H., Sakai, N., Kato, T. & Sugimoto, H. High voltage Cu_2ZnSnS_4 submodules by hybrid buffer layer. In *2013 IEEE 39th Photovoltaic Specialists Conference (PVSC)* https://doi.org/10.1109/PVSC.2013.6744281 (IEEE, 2013).
15. Kim, J. et al. High efficiency $Cu_2ZnSn(S,Se)_4$ solar cells by applying a double In_2S_3/CdS emitter. *Adv. Mater.* **26**, 7427–7431 (2014).
16. Hiroi, H., Sakai, N., Iwata, Y., Kato, T. & Sugimoto, H. Impact of buffer layer on kesterite solar cells. In *2015 IEEE 42nd Photovoltaic Specialist Conference (PVSC)* https://doi.org/10.1109/PVSC.2015.7356415 (IEEE, 2015).
17. Gang, M. G. et al. Sputtering processed highly efficient $Cu_2ZnSn(S,Se)_4$ solar cells by a low-cost, simple, environmentally friendly, and up-scalable strategy. *Green Chem.* **18**, 700–711 (2016).
18. Antunez, P. D., Bishop, D. M., Luo, Y. & Haight, R. Efficient kesterite solar cells with high open-circuit voltage for applications in powering distributed devices. *Nat. Energy* **2**, 884–890 (2017).
19. Xiang, C. et al. Solution-processed kesterite solar module with 10.1% certified efficiency. *Nat. Energy* **10**, 1315–1322 (2025).
20. Xu, X. et al. Alkali-metal-mediated control of phase segregation for flexible kesterite solar cells and modules with improved efficiency. *Nat. Energy* **11**, 854–865 (2026).
21. Shi, J. et al. Multinary alloying for facilitated cation exchange and suppressed defect formation in kesterite solar cells with above 14% certified efficiency. *Nat. Energy* **9**, 1095–1104 (2024).
22. Wang, A. et al. Cd-free pure sulfide kesterite Cu_2ZnSnS_4 solar cell with over 800 mV open-circuit voltage enabled by phase evolution intervention. *Adv. Mater.* **36**, 2307733 (2024).
23. Zhou, J. et al. Control of the phase evolution of kesterite by tuning of the selenium partial pressure for solar cells with 13.8% certified efficiency. *Nat. Energy* **8**, 526–535 (2023).
24. Kim, S.-Y. et al. Void and secondary phase formation mechanisms of CZTSSe using Sn/Cu/Zn/Mo stacked elemental precursors. *Nano Energy* **59**, 399–411 (2019).
25. Xu, X. et al. Controlling selenization equilibrium enables high-quality kesterite absorbers for efficient solar cells. *Nat. Commun.* **14**, 6650 (2023).
26. Yao, G. et al. Phase evolution extension of $Cu_2ZnSn(S,Se)_4$ absorber boosting the efficiency of kesterite solar cells to 14.99%. *ACS Energy Lett.* **10**, 2761–2769 (2025).

27. Wei, H. et al. Regulating hetero-nucleation enabling over 14% efficient kesterite solar cells. *Small* **20**, 2308266 (2024).
28. Gong, Y. et al. Identifying the origin of the V_{OC} deficit of kesterite solar cells from the two grain growth mechanisms induced by Sn^{2+} and Sn^{4+} precursors in DMSO solution. *Energy Environ. Sci.* **14**, 2369–2380 (2021).
29. Chen, B. et al. Blade-coated perovskites on textured silicon for 26%-efficient monolithic perovskite/silicon tandem solar cells. *Joule* **4**, 850–864 (2020).
30. Sun, Y. et al. In situ coordinated HTL strategy for high-performance and scalable perovskite solar cells. *Nat. Commun.* **16**, 9110 (2025).
31. Jimenez-Arguijo, A. et al. Formation pathway of high-efficiency kesterite solar cells fabricated through molecular ink chemistry. *Nat. Energy* **11**, 194–208 (2026).
32. Mao, Y. et al. 12.86% efficient $Cu_2ZnSn(S,Se)_4$ thin film solar cells via inkjet printing with 2-methoxyethanol-based air-stable precursor ink. *Adv. Funct. Mater.* **35**, 2416689 (2025).
33. Deng, Y. et al. Efficient kesterite solar cells via scalable doctor-blading of 2-methoxyethanol-based molecular ink. *Energy Environ. Mater.* **9**, e70252 (2026).
34. Su, Z. et al. Fabrication of Cu_2ZnSnS_4 solar cells with 5.1% efficiency via thermal decomposition and reaction using a non-toxic sol-gel route. *J. Mater. Chem. A* **2**, 500–509 (2014).
35. Evans, W. J., Greci, M. A. & Ziller, J. W. Utility of 2-methoxyethanol in the synthesis of polyeuropium complexes: $\{[Eu(OCH_2CH_2OMe)_2(OC_6H_3R_2\text{-}2,6)^-][H^+]\}_4$ (R=Me, ^{i}Pr) and $[EuAl_2(OCH_2CH_2OMe)_3Me_5]_2$. *Inorg. Chem.* **37**, 5221–5226 (1998).
36. Agbenyeke, R. et al. Correlating molecular precursor interactions with device performance in solution-processed $Cu_2ZnSn(S,Se)_4$ thin-film solar cells. *ACS Appl. Mater. Interfaces* **16**, 35315–35322 (2024).
37. Larramona, G. et al. Stability, reliability, upscaling and possible technological applications of kesterite solar cells. *J. Phys. Energy* **2**, 024009 (2020).
38. Liu, J. et al. Evolutionary manufacturing approaches for advancing flexible perovskite solar cells. *Joule* **8**, 944–969 (2024).
39. Li, Y. et al. Suppressing element inhomogeneity enables 14.9% efficiency CZTSSe solar cells. *Adv. Mater.* **36**, 2400138 (2024).
40. Fang, Y. X. et al. Tailoring precursor chemistry enabled room temperature-processed perovskite films in ambient air for efficient and stable solar cells with improved reproducibility. *Adv. Funct. Mater.* **33**, 2303674 (2023).
41. Nina, S., Rabiatul, A., Any, G. & Hari, S. Combination of Fourier transform infrared (FTIR) with chemometrics for halal authentication of face mask products made from gelatin. *BIO Web Conf.* https://doi.org/10.1051/bioconf/202414804004 (2024).
42. Gong, Y. et al. Sn^{4+} precursor enables 12.4% efficient kesterite solar cell from DMSO solution with open circuit voltage deficit below 0.30 V. *Sci. China Mater.* **64**, 52–60 (2021).
43. Clark, J. A. et al. Complexation chemistry in *N*,*N*-dimethylformamide-based molecular inks for chalcogenide semiconductors and photovoltaic devices. *J. Am. Chem. Soc.* **141**, 298–308 (2018).
44. Xin, H., Katahara, J. K., Braly, I. L. & Hillhouse, H. W. 8% efficient $Cu_2ZnSn(S,Se)_4$ solar cells from redox equilibrated simple precursors in DMSO. *Adv. Energy Mater.* **4**, 1301823 (2014).
45. Xu, X. et al. Efficient and composition-tolerant kesterite $Cu_2ZnSn(S,Se)_4$ solar cells derived from an in situ formed multifunctional carbon framework. *Adv. Energy Mater.* **11**, 2102298 (2021).
46. Fornasini, P. & Grisenti, R. On EXAFS Debye–Waller factor and recent advances. *J. Synchrotron Radiat.* **22**, 1242–1257 (2015).
47. Kuzmin, A. & Chaboy, J. EXAFS and XANES analysis of oxides at the nanoscale. *IUCrJ* **1**, 571–589 (2014).
48. Rode, B., Schwenk, C., Hofer, T. & Randolf, B. Coordination and ligand exchange dynamics of solvated metal ions. *Coord. Chem. Rev.* **249**, 2993–3006 (2005).
49. Yamanoi, T., Inoue, R. & Oda, Y. 2,3,4,6-Tetra-*O*-benzyl-1-*C*-phenyl-α-D-glucopyranosyl 2,3,4,6-tetra-*O*-benzyl-α-D-glucopyranoside. *Molbank* **2012**, M761 (2012).
50. Chen, W.-C. et al. Fabrication of $Cu_2ZnSnSe_4$ solar cells through multi-step selenization of layered metallic precursor film. *Thin Solid Films* **618**, 42–49 (2016).
51. Kapoor, R., Gupta, A., Kapoor, P. & Venugopalan, P. The synthesis, NMR (^{1}H, ^{13}C, ^{119}Sn) and IR spectral studies of some di-and tri-organotin (IV) sulfonates: X-ray crystal structure of $[(n\text{-}C_4H_9)_2Sn(OSO_2C_6H_4CH_3\text{-}4)_2{\cdot}2H_2O]$. *Appl. Organomet. Chem.* **17**, 607–615 (2003).
52. Alves, W. A., Antunes, O. A. & Hollauer, E. Raman spectroscopic study on the formation of an adduct of acetonitrile with formamide. *Vib. Spectrosc.* **40**, 257–262 (2006).
53. Hadjiivanov, K. I. et al. Power of infrared and Raman spectroscopies to characterize metal–organic frameworks and investigate their interaction with guest molecules. *Chem. Rev.* **121**, 1286–1424 (2021).
54. Nagata, M. K. C. T. et al. Correlation of solid state and solution coordination numbers with infrared spectroscopy in five-, six-, and eight-coordinate transition metal complexes of DOTAM. *Polyhedron* **114**, 299–305 (2016).
55. Yin, K. et al. Gradient bandgaps in sulfide kesterite solar cells enable over 13% certified efficiency. *Nat. Energy* **10**, 205–214 (2025).
56. Wang, J. et al. Pd (II)/Pd (IV) redox shuttle to suppress vacancy defects at grain boundaries for efficient kesterite solar cells. *Nat. Commun.* **15**, 4344 (2024).
57. Kim, G. Y. et al. Surface potential on grain boundaries and intragrains of highly efficient $Cu_2ZnSn(S,Se)_4$ thin-films grown by two-step sputtering process. *Sol. Energy Mater. Sol. Cells* **127**, 129–135 (2014).
58. Nicoara, N. et al. Effect of the KF post-deposition treatment on grain boundary properties in $Cu(In,Ga)Se_2$ thin films. *Sci. Rep.* **7**, 41361 (2017).
59. Shi, J., Li, D., Luo, Y., Wu, H. & Meng, Q. Opto-electro-modulated transient photovoltage and photocurrent system for investigation of charge transport and recombination in solar cells. *Rev. Sci. Instrum.* **87**, 123107 (2016).
60. Li, Y. M. et al. Exploiting electrical transients to quantify charge loss in solar cells. *Joule* **4**, 472–489 (2020).
61. Krückemeier, L., Liu, Z., Krogmeier, B., Rau, U. & Kirchartz, T. Consistent interpretation of electrical and optical transients in halide perovskite layers and solar cells. *Adv. Energy Mater.* **11**, 2102290 (2021).
62. Wheeler, S. et al. Transient optoelectronic analysis of the impact of material energetics and recombination kinetics on the open-circuit voltage of hybrid perovskite solar cells. *J. Phys. Chem. C* **121**, 13496–13506 (2017).
63. Huang, C. et al. Meniscus-modulated blade coating enables high-quality α-phase formamidinium lead triiodide crystals and efficient perovskite minimodules. *Joule* **8**, 2539–2553 (2024).
64. Yang, K.-J. et al. Flexible $Cu_2ZnSn(S,Se)_4$ solar cells with over 10% efficiency and methods of enlarging the cell area. *Nat. Commun.* **10**, 2959 (2019).
65. Yoon, J.-H. et al. Characterization of efficiency-limiting resistance losses in monolithically integrated $Cu(In,Ga)Se_2$ solar modules. *Sci. Rep.* **5**, 7690 (2015).
66. Bermudez, V. & Perez-Rodriguez, A. Understanding the cell-to-module efficiency gap in $Cu(In,Ga)(S,Se)_2$ photovoltaics scale-up. *Nat. Energy* **3**, 466–475 (2018).

Publisher's note Springer Nature remains neutral with regard to jurisdictional claims in published maps and institutional affiliations.

Springer Nature or its licensor (e.g. a society or other partner) holds exclusive rights to this article under a publishing agreement with the author(s) or other rightsholder(s); author self-archiving of the accepted manuscript version of this article is solely governed by the terms of such publishing agreement and applicable law.

© The Author(s), under exclusive licence to Springer Nature Limited 2026

Methods

Materials

CuCl (99.999%, Alfa), $Zn(OAc)_2$ (99.99%, Aladdin), $SnCl_4$ (99.998%, Macklin), AgCl (99.5%, Innochem), $CdCl_2$ (99.99%, Aladdin), 2-methoxyethanol (99.8%, Aladdin), formamide (99.5%, Innochem), thiourea (99.99%, Aladdin, recrystallized before using), LiCl (99.9%, Alfa), NaCl (99.998%, Alfa), Se pellets (99.999%, Zhong Nuo Advanced Material), $CdSO_4{\cdot}8/3H_2O$ (99.99%, Aladdin), ammonium chloride (≥99.5%, Sinopharm Chemical Reagent) and ammonia (25.0% – 28.0%, Sinopharm Chemical Reagent) were used in this work. These chemicals except thiourea were used directly without further purification.

Precursor solution

The precursor solution was prepared as follows: first, thiourea was dissolved in the solvent, followed by the addition of CuCl, which was then dissolved with stirring to yield a colourless solution. Subsequently, AgCl was introduced into this solution and stirred for 1 h to obtain solution 1. Second, the solvent was added to a bottle containing $SnCl_4$ to produce a colourless solution. $Zn(OAc)_2$ and $CdCl_2$ were then dissolved in the Sn-containing solution to form solution 2. Third, solutions 1 and 2 were mixed to give the final precursor solution. In the precursor solution, the concentrations of metal elements and thiourea are 1.88 M and 3.20 M, respectively. The molar ratio of (Ag + Cu)/(Zn + Cd + Sn), (Zn + Cd)/Sn, Ag/(Ag + Cu), Cd/(Cd + Zn) and thiourea/metal are 0.75, 1.12, 0.10, 0.06 and 1.7, respectively. The control solution was prepared using MOE as the sole solvent. For the target solution, solution 1 was prepared in MOE and solution 2 was prepared in FA. The volume ratio of FA to MOE in the target precursor solution was 1:1. The incorporation of alkali metals have been described in detail in previous studies[11,20].

Precursor film preparation

The Mo substrates were cleaned using dish soap and deionized water, followed by N_2-flow drying, and then treated by UV-ozone for 15 min. The kesterite precursor films were prepared by blade-coating the precursor solution onto the cleaned Mo substrates with a blade gap set to 500 μm and a coating speed of 10 mm s^{-1}, followed by annealing on a 280 °C hot plate in air. The coating and annealing procedures were iteratively performed to achieve a target thickness of approximately 2 μm for the precursor films.

Selenization

The precursor film was cut into 2 × 2 cm^2 (4 × 4 cm^2 for modules) pieces and placed into the graphite box for a selenization treatment at 545 °C under nitrogen for 20 min, completing the absorber preparation process. Mg was also introduced as described in a previous study[6].

Cell fabrication

A 40–50-nm thick CdS buffer layer was deposited on the top of CZTSSe films by the chemical bath deposition method (70 °C, 0.614 g $CdSO_4$, 0.128 g NH_4Cl, 0.7288 g thiourea and 10.5 ml ammonia in 200 ml H_2O), followed by sputtering an ~50 nm i-ZnO layer (target diameter: 75 mm, sputtering power: 55 W, gas source: Ar, pressure: ~2 Pa and temperature: 60 °C) and a 200 nm indium tin oxide (ITO) layer (target diameter: 75 mm, sputtering power: 60 W, gas source: Ar, pressure: ~0.2 Pa, temperature: 160 °C). Then ~50 nm nickel (Ni) and ~2 μm aluminium (Al) were evaporated on the ITO layer. Finally, an ~110 nm MgF_2 layer covered the whole device, serving as the anti-reflection coating. Small cells were separated from each other by mechanical scribing and the designed area of an individual cell is ~0.25 cm^2. In addition, the large-area device was fabricated as a single cell with a designated illuminated area of ~1.08 cm^2.

Module fabrication

Module fabrication followed the same materials preparation as the small-area cells; the only difference was the incorporation of designed interconnect scribes (P1–P3). Before depositing the precursor films, the P1 (80 μm) scribe was performed with a nanosecond-pulsed laser to remove the Mo back contact. After sputtering ZnO, the P2 (120 μm) scribe was executed with the same nanosecond laser to ablate all layers above Mo and expose the Mo for series interconnection. Following ITO deposition, the P3 (100 μm) scribe was completed by mechanical scribing to remove the layers above Mo and isolate the front contact. The total channel width is approximately 400 μm. The Ni/Al grid electrode and MgF_2 layer were also deposited to enhance the lateral conductivity and to reduce reflectivity. The final monolithic module consisted of 6 series-connected subcells, yielding a total area of ~10.5 cm^2 and dead zone of ~0.9 cm^2.

Material and device characterization

Raman spectroscopy was conducted using a LabRAM HR Evolution (HORIBA) spectrometer, with a 532 nm laser as the excitation source. SEM images were measured on Hitachi S4800. Steady-state photoluminescence spectra were obtained from a photoluminescence spectrometer (Edinburgh Instruments, FLS 920), excited with a picosecond-pulsed diode laser (EPL-640) with the wavelength of 638.2 nm while cooling with liquid helium. The value was obtained from high-resolution camera imaging followed by colour analysis. Thermogravimetric analysis was performed using a TGA Q5000 V3.17 Build 265 (TA Instruments) thermal analyser.

The *J*–*V* characteristics of the photovoltaic cells were measured using a Keithley 2601 Source Meter under simulated AM 1.5 G solar illumination at an intensity of 100 mW cm^{-2}. Calibration was performed using a silicon reference cell, which was calibrated by the National Institute of Metrology of China. The voltage sweep ranged from −50 mV to 600 mV (−50 mV to 4,000 mV for modules) at a scan rate of approximately 90 mV s^{-1}. Cell certification was performed at the NPVM, confirming a certified aperture area of 1.075 cm^2 for the cell and 10.51 cm^2 for the module. All measurements were conducted under ambient conditions (air, 25 °C and uncontrolled humidity), with no preconditioning steps prior to the measurements. The EQE was determined using an Enlitech QE-R system, which used calibrated silicon (Si) and germanium (Ge) diodes for reference. Modulated transient photocurrent and photovoltage (M-TPC/TPV) measurements were obtained by a tunable nanosecond laser pumped at 640 nm and recorded by a subnanosecond resolved digital oscilloscope (Tektronix, DPO 7104) with a sampling resistance of 50 Ω or 1 MΩ. Electroluminescence characterization was performed using a vis-NIR complementary metal-oxide semiconductor camera (Spark-Opt, CIS-CM990) covering a spectral range of 400–1,700 nm.

Reporting summary

Further information on research design is available in the Nature Portfolio Reporting Summary linked to this article.

Data availability

The main data supporting the findings of this study are available within the main text and Supplementary Information. Source data are provided with this paper.

Acknowledgements

We thank the ID46(HEPS)-X-Ray Absorption Spectroscopy Beamline of High Energy Photon Source (https://cstr.cn/31138.02.HEPS.ID46), L. Zheng and F. Zhan for providing technical support and assistance in XAFS data collection and analysis. We gratefully acknowledge B. Wang at Institute of Physics, Chinese Academy of Sciences, for assistance with the mass spectrometry measurements. We also acknowledge the Excellent Science and Technology Innovation Group of Jiangsu Province at Nanjing University of Science and Technology for their help in theoretical calculations.

Author contributions

B.Z., J.S. and Q.M. conceived of the idea, proposed the theoretical mechanism and designed the experiments. B.Z., M.J., X.X. and J.Z. performed the experiments and data analysis. Jinlin Wang, T.G., Yuan Li and S.C. supported CZTSSe solar cell fabrication. Jingchen Wang supported the colour value analysis. Yiming Li participated in photoelectric characterization. H.W. and Yanhong Luo supported the discussion. B.Z., J.S. and Q.M. participated in writing and revising the paper. All authors discussed the results and approved the paper.

Funding

This work was supported by the National Key R&D Program of China (2024YFB4205000), National Natural Science Foundation of China (52222212, 52227803, 52172261 and 52402243), Zhejiang Provincial Natural Science Foundation (LQN25E020011). J.S. also gratefully acknowledges the support from the Youth Innovation Promotion Association of the Chinese Academy of Sciences (2022006).

Competing interests

The authors declare no competing interests.

Additional information

Supplementary information The online version contains supplementary material available at https://doi.org/10.1038/s41563-026-02703-6.

Correspondence and requests for materials should be addressed to Jiangjian Shi or Qingbo Meng.

Peer review information *Nature Materials* thanks Stela Canulescu and the other, anonymous, reviewer(s) for their contribution to the peer review of this work.

Reprints and permissions information is available at www.nature.com/reprints.

nature portfolio

Corresponding author(s): Qingbo Meng, Jiangjian Shi

Solar Cells Reporting Summary

Nature Portfolio wishes to improve the reproducibility of the work that we publish. This form is intended for publication with all accepted papers reporting the characterization of photovoltaic devices and provides structure for consistency and transparency in reporting. Some list items might not apply to an individual manuscript, but all fields must be completed for clarity.

For further information on Nature Research policies, including our data availability policy, see Authors & Referees.

Experimental design

Please check the following details are reported in the manuscript, and provide a brief description or explanation where applicable.

1. Dimensions

Area of the tested solar cells	☒ Yes	The area is 1.075 cm2 for cells and 10.51 cm2 for modules, which is given in experimental section and certification reports.
	☐ No	*Explain why this information is not reported/not relevant.*
Method used to determine the device area	☒ Yes	The device area is determined by masks and it is given in experimental section and certification reports.
	☐ No	*Explain why this information is not reported/not relevant.*

2. Current-voltage characterization

Current density-voltage (J-V) plots in both forward and backward direction	☒ Yes	The forward and backward scan J-V curves are given in certification reports showing no hysteresis
	☐ No	
Voltage scan conditions	☒ Yes	The voltage was forward scanned from -50 mV to 600 mV for cells and -50 mV to 4000 mV for modules with a scanning rate of 90 mV·s-1.
	☐ No	*Explain why this information is not reported/not relevant.*
Test environment	☒ Yes	The J-V tests were conducted in air at 25 °C. The test environment is given in experimental section.
	☐ No	*Explain why this information is not reported/not relevant.*
Protocol for preconditioning of the device before its characterization	☒ Yes	No preconditioning of the device was before the measurement. This is given in experimental section.
	☐ No	*Explain why this information is not reported/not relevant.*
Stability of the J-V characteristic	☐ Yes	*Provide a description of the method used. The stability of the J-V characteristic can be verified with time evolution of the maximum power point or with the photocurrent at maximum power point; see ref. 5 for details.*
	☒ No	Kesterite solar cells do not have hysteresis. And in the certification process, maximum power output had been traced for several minutes to confirm the cell efficiency.

3. Hysteresis or any other unusual behaviour

Description of the unusual behaviour observed during the characterization	☐ Yes	*Provide a description of hysteresis or any other unusual behaviour observed during the characterization.*
	☒ No	Kesterite solar cells do not have hysteresis or other unusual behavior.
Related experimental data	☐ Yes	*Provide a description of the related experimental data.*
	☒ No	Kesterite solar cells do not have hysteresis or other unusual behavior.

4. Efficiency

External quantum efficiency (EQE) or incident photons to current efficiency (IPCE)	☒ Yes	Given in Fig. 4c
	☐ No	*Explain why this information is not reported/not relevant.*

A comparison between the integrated response under the standard reference spectrum and the response measure under the simulator	☒ Yes ☐ No	The integrated JSC from EQE spectra supports the results of the J-V measurements. *Explain why this information is not reported/not relevant.*
For tandem solar cells, the bias illumination and bias voltage used for each subcell	☐ Yes ☒ No	*Provide a description of the measurement conditions.* No tandem solar cell was studied

5. Calibration

Light source and reference cell or sensor used for the characterization	☒ Yes ☐ No	The J-V curves of the solar cells were measured by using Keithley Source Meter under simulated AM 1.5 sunlight at 100 mW·cm-2 calibrated with Si reference cell. This is given in experimental section. *Explain why this information is not reported/not relevant.*
Confirmation that the reference cell was calibrated and certified	☒ Yes ☐ No	The reference cell was calibrated by National Institute of Metrology, China. This is given in supplementary Information. *Explain why this information is not reported/not relevant.*
Calculation of spectral mismatch between the reference cell and the devices under test	☒ Yes ☐ No	The mismatch is 1.011 for cells and 1.005 for modules, given in certification reports in supplementary information. *Explain why this information is not reported/not relevant.*

6. Mask/aperture

Size of the mask/aperture used during testing	☒ Yes ☐ No	The mask area is 1.075 cm2 for cells and 10.51 cm2 for modules, given in certification reports. *Explain why this information is not reported/not relevant.*
Variation of the measured short-circuit current density with the mask/aperture area	☐ Yes ☒ No	*Report the difference in the short-circuit current density values measured with the mask and aperture area.* No such phenomenon in kesterite solar cells

7. Performance certification

Identity of the independent certification laboratory that confirmed the photovoltaic performance	☒ Yes ☐ No	The photovoltaic performance is certified in NPVM. *Explain why this information is not reported/not relevant.*
A copy of any certificate(s)	☒ Yes ☐ No	The certification reports are given in supplementary information. *Explain why this information is not reported/not relevant.*

8. Statistics

Number of solar cells tested	☒ Yes ☐ No	24 cells are used for statistic analysis. *Explain why this information is not reported/not relevant.*
Statistical analysis of the device performance	☒ Yes ☐ No	Statistical analysis of the device performance is given in Fig. 1, Fig.4 and Supplementary Figs. 1,2,27,28. *Explain why this information is not reported/not relevant.*

9. Long-term stability analysis

Type of analysis, bias conditions and environmental conditions	☐ Yes ☒ No	*Provide a description of the type of analysis, bias conditions and environmental conditions (e.g. illumination type, temperature, atmosphere humidity, encapsulation method, preconditioning temperature, bias) for each long-term stability analysis carried out; see ref. 7 and 8 for details.* No stability problem has been reported in kesterite solar cells.